

Double Supersolid Phase in a Bosonic t - J - V Model with Rydberg Atoms

Kuangjie Chen,^{1,2} Yang Qi,^{1,3} Zheng Yan,^{4,5,*} and Xiaopeng Li^{1,2,6,3,†}

¹State Key Laboratory of Surface Physics, Institute of Nanoelectronics and Quantum Computing, Department of Physics, Fudan University, Shanghai 200438, China

²Shanghai Qizhi Institute and Shanghai Artificial Intelligence Laboratory, Xuhui District, Shanghai 200232, China

³Hefei National Laboratory, Hefei 230088, China

⁴Department of Physics, School of Science and Research Center for Industries of the Future, Westlake University, Hangzhou 310030, China

⁵Institute of Natural Sciences, Westlake Institute for Advanced Study, Hangzhou 310024, China

⁶Shanghai Research Center for Quantum Sciences, Shanghai 201315, China

Recent advances in Rydberg tweezer arrays bring novel opportunities for programmable quantum simulations beyond previous capabilities. In this work, we investigate a bosonic t - J - V model currently realized with Rydberg atoms. Through large-scale quantum Monte Carlo simulations, we uncover an emergent double supersolid (DSS) phase with the coexistence of two superfluids and crystalline order. Tunable long-range tunneling and repulsive hole-hole interactions enable a rich phase diagram featuring a double superfluid phase, a DSS phase, and an antiferromagnetic insulator. Intriguingly, within the DSS regime we observe an unconventional thermal enhancement of crystalline order. Our results establish the bosonic t - J - V model as a promising and experimentally accessible platform for exploring exotic quantum phases in Rydberg atom arrays.

Introduction.— The pursuit of understanding exotic quantum phases has led to significant interest in systems where competing interactions give rise to rich phase diagrams. Rydberg atom arrays, especially those arranged in optical tweezers, offer a versatile platform for simulating quantum many-body systems. The ability to engineer long-range interactions and precise control over individual atoms has facilitated the realization of various quantum models, thanks to the immense experimental progress over the last decade [1–8].

A large theme of Rydberg atom array experiments focus on spin-1/2 models, including transverse field Ising [9] and quantum XY [10] models with dipolar or van der Waals interactions. These systems have enabled the observation of a variety of exotic phases, such as topological orders [3], quantum scar states [11], continuous symmetry breaking [12] and quantum floating phases [13]. At the same time, quantum simulations of doped quantum magnetism [14] are of great interest in condensed matter physics, for modeling more complex quantum phenomena. A prominent example is the hole-doped spin-1/2 model [15], whose understanding is expected to be critical to characterizing high- T_c superconductivity [16–19].

A concrete system to study the interplay of spin fluctuations and hole doping is the bosonic t - J - V model [15], recently realized in a Rydberg atom array [20]. In this implementation, three Rydberg states of ^{87}Rb atoms— $|61S_{1/2}, m_J = 1/2\rangle$, $|60S_{1/2}, m_J = 1/2\rangle$, and $|60P_{3/2}, m_J = -1/2\rangle$ —encode spin-up ($|\uparrow\rangle$), spin-down ($|\downarrow\rangle$), and hole ($|h\rangle$), respectively. The dipolar interactions mediate long-range hole tunneling, while the van der Waals interactions generate both spin-spin and hole-hole interactions. The relative interaction strengths are widely tunable by controlling the quantization axis and tweezer array geometry. Unlike the conventional electronic t - J model, where the spin exchange is necessarily antiferromagnetic in the strong coupling limit, the atomic system permits access to fascinating regimes featuring hole-dynamics in both antiferromagnetic and ferromagnetic spin backgrounds, accompanied by long-range interactions. Theoretical inves-

tigations of the quantum phases emerging from the complex interplay of spin exchange, hole dynamics and long-range interactions are crucial for advancing quantum simulations in this experimental platform.

In this Letter, we present a first study of the ground-state phase diagram of the bosonic t - J - V model on the square lattice using quantum Monte Carlo. Under strong hole-hole repulsion, the system exhibits conventional antiferromagnetic (AFM) and double superfluid (DSF) phases at small and large tunneling (t) limits, respectively. At intermediate t , we uncover an intriguing double supersolid (DSS) phase—an exotic state characterized by spontaneous breaking of the lattice symmetry and two $U(1)$ symmetries. This DSS phase emerges from the intricate interplay between long-range tunneling, hole-hole repulsion and strong spin-hole couplings. These characteristic signatures are directly accessible to current Rydberg tweezer arrays. Further experimental studies of DSS phenomena are expected to contribute strongly to the fundamental understanding of doped quantum magnetism, of direct relevance to high- T_c superconductivity [5, 19, 21–28].

Model.— We investigate the bosonic t - J - V model describing Rydberg atoms on the two-dimensional (2D) square lattice with the following Hamiltonian [20],

$$\begin{aligned}\hat{H}_{tJV} &= \hat{H}_t + \hat{H}_J + \hat{H}_V, \\ \hat{H}_t &= - \sum_{i<j} \sum_{\sigma=\downarrow,\uparrow} \frac{t_\sigma}{r_{ij}^3} \left(\hat{a}_{i,\sigma}^\dagger \hat{a}_{j,h}^\dagger \hat{a}_{i,h} \hat{a}_{j,\sigma} + \text{h.c.} \right), \\ \hat{H}_J &= \sum_{i<j} \frac{1}{r_{ij}^6} \left[J^z \hat{S}_i^z \hat{S}_j^z + \frac{J^\perp}{2} \left(\hat{S}_i^+ \hat{S}_j^- + \text{h.c.} \right) \right], \\ \hat{H}_V &= \sum_{i<j} \frac{V}{r_{ij}^6} \hat{n}_i^h \hat{n}_j^h - \mu \sum_j \hat{n}_j^h.\end{aligned}\quad (1)$$

The effective spin-1/2 and hole states (Fig. 1(a)) correspond to three Rydberg atomic levels with r_{ij} denoting the distance between site i and j . The coupling t_σ describes the dipolar tunneling between states with different parity. The

J^z and V terms represent the diagonal van der Waals interactions between Rydberg pairs, while the J^\perp term corresponds to the off-diagonal van der Waals interactions between $|nS, (n+1)S\rangle$ pairs. The Schwinger bosons operators, $\hat{a}_{j,h}^\dagger$ and $\hat{a}_{j,\sigma}^\dagger$, create a hole and a spin σ on site j , respectively. The local hole number and spin number operator at site j is given by $\hat{n}_j^h = \hat{a}_{j,h}^\dagger \hat{a}_{j,h}$ and $\hat{n}_j^\sigma = \hat{a}_{j,\sigma}^\dagger \hat{a}_{j,\sigma}$. The spin-1/2 operators are given by $\hat{S}_j^\gamma = \frac{1}{2} \hat{a}_{j,\alpha}^\dagger \sigma_{\alpha\beta}^\gamma \hat{a}_{j,\beta}$ with $\gamma \in \{x, y, z\}$ and σ^γ being the Pauli matrix. The chemical potential μ is introduced to control the hole filling in the system. We focus at $\mu = 0$ in this study. Due to the local Hilbert space constraint of the Schwinger bosons, $\hat{n}_j^\uparrow + \hat{n}_j^\downarrow + \hat{n}_j^h = 1$, the Hamiltonian (1) respects two global $U(1)$ symmetries, corresponding to the conservation of hole dopants, $\hat{N}_h = \sum_j \hat{n}_j^h$, and total magnetization, $\hat{S}_{tot}^z = \sum_j \hat{S}_j^z$.

In our simulation, we set $t_\uparrow = t_\downarrow = t$, $J^z = 4$ and $J_\perp = -1$ (energy unit), for which the model is sign-problem-free. We focus on repulsive hole-hole interactions ($V \geq 0$) and explore the phase diagram using the stochastic series expansion (SSE) QMC method with the directed-loop algorithm [29–31]. Our simulations are performed on $L \times L$ square lattices with periodic boundary conditions (PBC), with inverse temperature $\beta = L$ to probe ground state properties. The simulations present significant challenges due to the long-range van der Waals and dipolar interactions, and lack of efficient quantum fluctuations at small- t . We employ annealing techniques [8, 32–34] and develop QMC algorithms for the bosonic t - J - V model that are efficient across a wide parameter range. The consequent phase diagram is shown in Fig. 1(b). Our results reveal: (i) an antiferromagnetic phase and a double superfluid phase (spin in-plane order + hole-superfluidity) separated by a first-order transition at $V \lesssim 3.0$, (ii) an emergent double supersolid phase (co-existing ferromagnetic in-plane and antiferromagnetic out-of-plane spin orders + hole superfluidity) between these phases when $V \gtrsim 3.0$, with its stable region widening systematically as V increases. At finite temperature, the DSS phase displays a striking non-monotonic response with increasing temperature. We attribute this to a ‘‘thermal compensation ordering’’ mechanism, which will be discussed in detail below.

AFM-to-DSF transition.— To characterize different phases, we consider the AFM order parameter $|m_z| = \frac{1}{N} \langle |\sum_j e^{i\mathbf{Q}\cdot\mathbf{r}_j} S_j^z| \rangle$ and the spin structure factor $S(\mathbf{Q}) = \frac{1}{N} \sum_{j,k} e^{i\mathbf{Q}\cdot(\mathbf{r}_j - \mathbf{r}_k)} \langle S_j^z S_k^z \rangle$ at the ordering vector $\mathbf{Q} = (\pi, \pi)$. We note that for the hole $\langle h_j | \hat{S}_j^z | h_j \rangle = 0$. The AFM phase that breaks the lattice translation symmetry is indicated by a non-vanishing $|m_z|$ (or $S(\pi, \pi)/N$) in the thermodynamic limit. The superfluidity (associated with the $U(1)$ symmetry breaking of holes) is distinguished by a nonzero superfluid density $\rho_s = L^{2-d} \langle W_x^2 + W_y^2 \rangle / 2d\beta t$, d is the dimension of system and $W_{x/y}$ are the winding numbers of bosonic holes’ worldlines in the x - and y -directions [35].

During our numerical simulations, we encountered challenges with conventional QMC methods when dealing with strong first-order transitions between the AFM and DSF

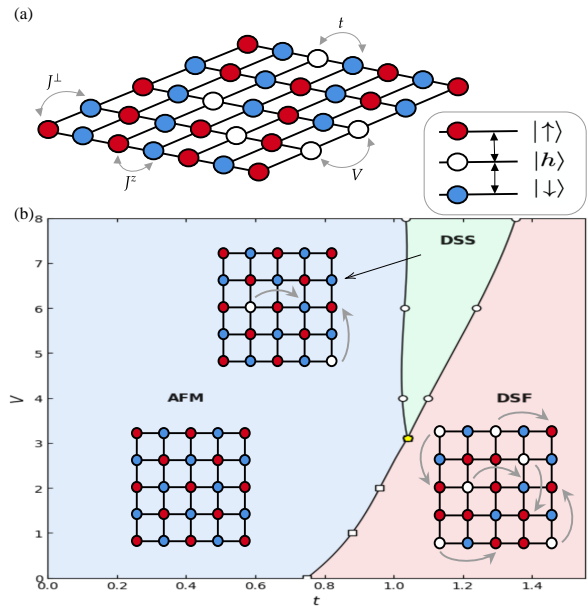


FIG. 1: (Color online) (a) Illustration of the bosonic t - J - V model on a square lattice. The spin-1/2 and hole degrees of freedom are encoded in three distinct Rydberg states, represented by red ($|\uparrow\rangle$), blue ($|\downarrow\rangle$), and white ($|h\rangle$) circles. Effective tunneling t , spin-spin interactions J^z , J^\perp , and hole-hole interactions V emerge from the interactions among these Rydberg states. (b) Ground-state phase diagram of the t - J - V model in the t - V plane at fixed parameters $J^z = 4$, $J^\perp = -1$, and chemical potential $\mu = 0$. The phase diagram contains an AFM phase (blue region), a double superfluid (DSF) phase (red region), and a double supersolid (DSS) phase (green region). Insets provide schematic illustrations of each phase, with solid lines indicating phase boundaries.

phases. The performance of the directed-loop algorithm is further compromised at small t due to the weak quantum fluctuations. To overcome these challenges, we employed the annealing method [8], starting with a large- t value in the DSF region and gradually decreasing t during the simulation. Once in the AFM region, we reversed the process by incrementally increasing t . The results, shown in Fig. 2, reveal that the forward and backward annealing processes yield different outcomes in the intermediate region. This hysteresis loop indicates that the simulation trajectories retain memory of the initial state. Combined with the discontinuous jumps in hole density, $\rho = \frac{1}{N} \langle \sum_j \hat{n}_j^h \rangle$, as t varies, these results confirm a first-order phase transition between the AFM and DSF phases. We thus identified the precise phase transition point by locating the kink where the derivative of the minimum energy shows a discontinuity (Fig. 2(a)).

DSS phase.— We now focus on the large- V region. Our previous results show that increasing the tunneling t causes holes to proliferate coherently, eventually destroying the AFM order in the small- V region. To stabilize both AFM order and superfluidity simultaneously, we increase V , creating strong

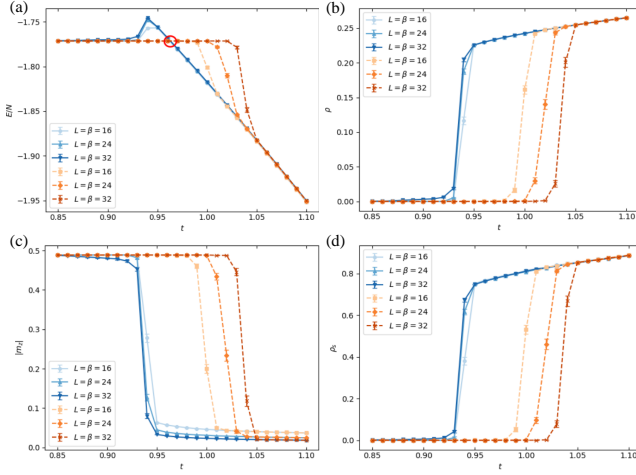


FIG. 2: (Color online) (a) The ground-state energy per site E/N , (b) the hole density ρ , (c) the AFM order parameter $|m_z|$, and (d) the superfluid density ρ_s as functions of the tunneling strength t for various system sizes. The blue solid lines represent the annealing forward results, while the yellow dashed lines correspond to the annealing backward results. The hole-hole repulsion strength is set to $V = 2$.

hole-hole repulsion that suppresses the hole density. This leads to the emergence of a DSS phase characterized by the crystalline order and breaking of two $U(1)$ symmetries.

We set the parameter $V = 8$, which gives a strong blockade effect to the hole. The QMC simulations are still performed via the annealing protocol. The hysteresis behavior that happened at weak repulsion regime now disappears. In addition to the spin structure factor and superfluid density, we measure the fidelity susceptibility, which provides a direct method for detecting quantum phases and phase transitions. For a general Hamiltonian $\hat{H}(\lambda) = \hat{H}_0 + \lambda\hat{H}_1$, where λ is the parameter driving the phase transition, the fidelity susceptibility at finite temperature is defined as [36–39]:

$$\chi_F(\lambda) = \int_0^{\beta/2} \tau [\langle \hat{H}_1(\tau)\hat{H}_1 \rangle - \langle \hat{H}_1 \rangle^2] d\tau, \quad (2)$$

where $\langle \cdot \cdot \rangle$ denotes the thermal average at inverse temperature β and $\hat{H}_1(\tau) = e^{\tau\hat{H}} \hat{H}_1 e^{-\tau\hat{H}}$. In our SSE simulations, the tunneling strength t serves as the driving parameter, and χ_F is extracted by monitoring the \hat{H}_t operators during the imaginary time evolution.

The results are shown in Fig. 3. The first-order transition that separates the AFM and DSF phases at weak hole-repulsion, is now replaced by an intermediate DSS phase in the middle from $t \simeq 1.035$ to $t \simeq 1.354$, where both of $S(\pi, \pi)/N$ and ρ_s are finite. The fidelity susceptibility per site χ_F/N provides additional support for the phase transition. As shown in Fig. 3(b), it approaches zero deep inside both the AFM and DSS phases, but exhibits a sharp increase at the AFM-to-DSS transition, forming a clear plateau throughout the DSS phase. This plateau indicates the increased sen-

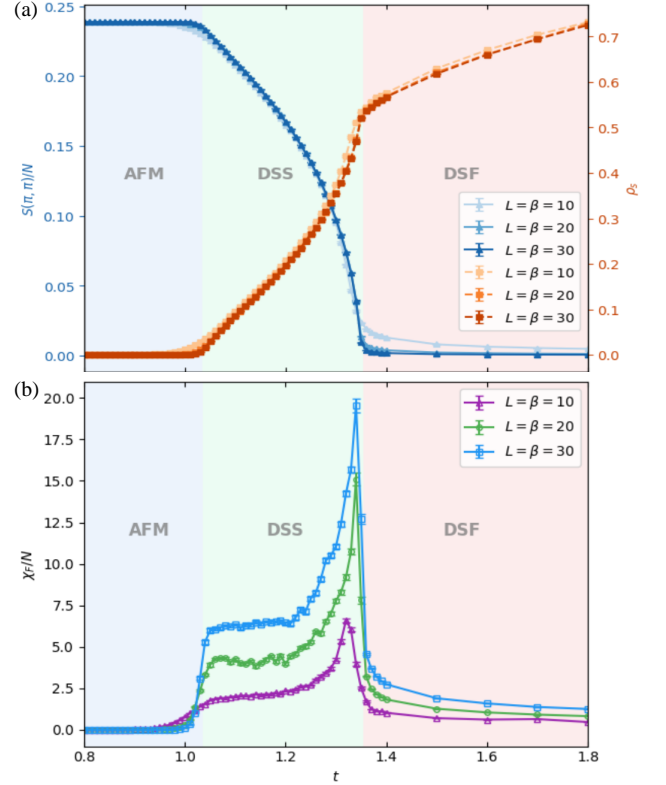


FIG. 3: (Color online) (a) The structure factor $S(\pi, \pi)/N$ (blue solid lines) and the superfluid density ρ_s (yellow dashed lines) as functions of the tunneling strength t are shown for various system sizes. (b) The fidelity susceptibility per site χ_F/N for different system sizes, identifying the transitions from AFM to DSS and from DSS to DSF. The hole-hole repulsion strength is set to $V = 8$.

sitivity of the DSS to the variations of the tunneling strength t . As t increases further, χ_F/N shows a divergent peak at the DSS-to-DSF transition with increasing system size. This behavior is fully consistent with our order parameter results.

To directly validate the lattice symmetry breaking and the $U(1)$ symmetry breaking of the total magnetization, we further calculate the equal-time diagonal spin correlation functions $C^z(\mathbf{r}) = \frac{1}{N} \sum_i \langle S_i^z S_{i+\mathbf{r}}^z \rangle$ and the off-diagonal spin correlation functions $C^{xy}(\mathbf{r}) = \frac{1}{2N} \sum_i \langle S_i^x S_{i+\mathbf{r}}^x + S_i^y S_{i+\mathbf{r}}^y \rangle$ in the DSS phase (Fig. 4 (a) and (b)) and in the DSF phase (Fig. 4 (c) and (d)). The non-vanishing diagonal and off-diagonal spin correlations indicate that the spin part exhibits both the AFM out-of-plane and FM in-plane order in the DSS region, which can be experimentally verified by measuring the diagonal correlations $\langle S_i^z S_j^z \rangle$ and the in-plane correlations $\langle S_i^x S_j^x \rangle$ in the Rydberg tweezer arrays. The DSS here can be understood in the context of the defect mechanism proposed by Andreev-Lifshitz-Chester (ALC) [40, 41]. In the ALC framework, supersolidity emerges when vacancies or defects (holes) coherently delocalize within an otherwise ordered crystal, originating from the competitions between the

kinetic energy gain through hole delocalization and the potential energy cost of distorting the crystalline order. Finite-size scaling analysis of phase transitions can be appreciated from the SM [42].

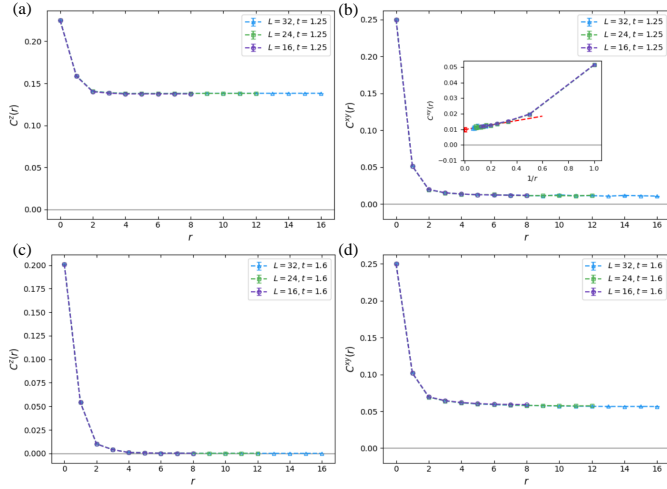


FIG. 4: (Color online) The diagonal spin correlations $|C^z(\mathbf{r})|$ and off-diagonal spin correlations $C^{xy}(\mathbf{r})$ with $\mathbf{r} = (r, 0)$, are shown in the DSS region (panels (a) and (b), $t = 1.25$) and the DSF region (panels (c) and (d), $t = 1.6$). In the inset of panel (b), $C^{xy}(\mathbf{r})$ is plotted against $1/r$ and the red dashed line denotes a linear fit using the finite-size ($L = 32$) data for $r \geq 4$, to extrapolate to $1/r = 0$. $V = 8$.

Finite-temperature transition.— To investigate the thermal stability of the DSS phase, we conduct finite-temperature QMC simulations with parameters $V = 8$ and $t = 1.2$, which lies within the DSS region identified in Fig. 3 in the ground state. We employ the thermal annealing method [43, 44], starting with high temperature in the disordered phase and then gradually decreasing temperature. The structure factor $S(\pi, \pi)/N$ and the superfluid density ρ_s along the annealing path are shown in Fig. 5 (a). At low temperatures, both $S(\pi, \pi)/N$ and ρ_s remain finite, confirming the thermal stability of the DSS phase. As the temperature increases, the superfluid density diminishes first, vanishing at approximately $T \simeq 0.5$ through a BKT transition. This transition transforms the DSS into a hole-doped AFM insulating phase with persistent diagonal order but zero superfluid density (The examination of the spin superfluidity is shown in the SM [42]). As we increase the temperature further, the AFM order eventually melts at $T \simeq 1.13$, yielding a completely disordered phase, which is consistent with the 2D Ising-type transition [42].

A remarkable feature of the DSS phase is the anomalous response of its spin structure factor to increasing temperature. In the temperature regime of $T \lesssim 0.5$, the spin structure factor $S(\pi, \pi)/N$ increases anomalously with temperature, instead of being suppressed by thermal fluctuations. This counterintuitive phenomenon emerges from an intricate interplay between spin and hole degrees of freedom. From Fig. 5(b),

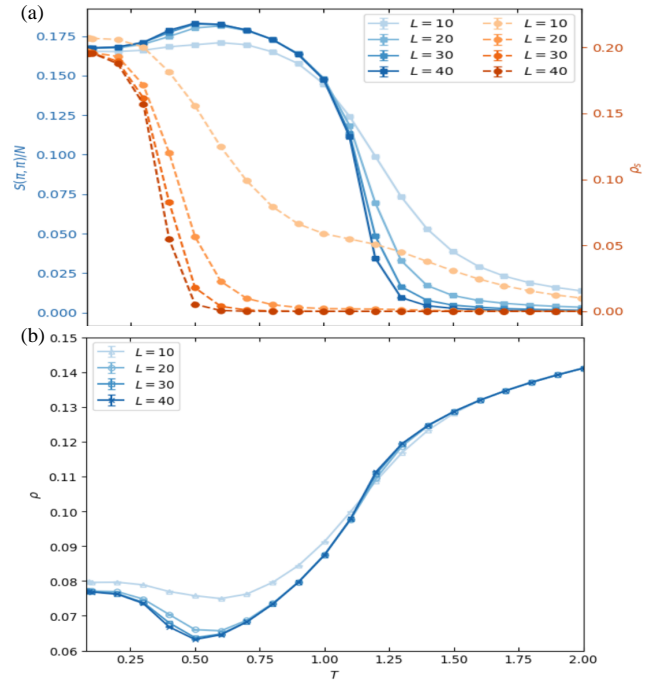


FIG. 5: (Color online) (a) The structure factor $S(\pi, \pi)/N$ (blue solid lines) and the superfluid density ρ_s (yellow dashed lines) as functions of temperature T . (b) The hole density ρ versus temperature T is shown for the same four system sizes. All data were obtained for $V = 8$ and $t = 1.2$.

the anomalous thermal response of $S(\pi, \pi)/N$ is tied with the non-monotonic behavior of the hole density, which shows a minimum at $T \simeq 0.5$. This reduction in the hole density strengthens the spin-spin correlations. The hole density decrease originates from the loss of superfluidity near the BKT transition temperature, which localizes the holes and increases their effective mass to enforce a sparser distribution, thereby reducing their disruption to the spin background. This phenomenon, dubbed “thermal compensation ordering”, demonstrates how thermal fluctuations can actually enhance ordering in systems with multiple coupled degrees of freedom rather than universally destroying it. Such non-monotonic behavior stems from the competition between spin and hole degrees of freedom—an intricate effect absent in simpler two-level systems at finite temperature.

Experimental protocols.— The Hamiltonian in Eq. (1) conserves the hole dopants $\hat{N}_h = \sum_j \hat{n}_j^h$ and the total magnetization $\hat{S}_{tot}^z = \sum_j \hat{S}_j^z$ [20]. While our QMC simulations employ a grand canonical ensemble, the hole density ρ and total magnetization S_{tot}^z fluctuate during simulations to find minimum energy configurations. Our theoretical predictions can be directly verified in Rydberg atom array experiments through the following protocol: (i) Initialize the system with specific hole density ρ and magnetization S_{tot}^z by precisely controlling site-specific laser intensities and detunings to match our numerical predictions; (ii) Rapidly quench the detuning to zero [20, 45]

to confine the system within the desired ρ and S_{tot}^z sectors; (iii) Allow the system to evolve under \hat{H}_{tJV} until equilibrium is reached, exploiting the long coherence times characteristic of Rydberg atoms; (iv) Perform projective measurement to evaluate the diagonal and off-diagonal correlations, providing direct experimental signatures of the DSS phase.

Conclusion.— In summary, we have investigated the bosonic t - J - V model on a square lattice using large-scale QMC simulations, motivated by its recent realization in Rydberg atom array [20]. We identified a rich ground-state phase diagram comprising both conventional AFM and DSF phases, as well as an exotic DSS phase. The DSS phase emerges from the interplay between spin and hole degrees of freedom under long-range interactions, characterized by simultaneous breaking of the lattice symmetry and two $U(1)$ symmetries, appearing above a critical hole-hole repulsion. Furthermore, we analyzed the thermal stability of the DSS phase, revealing a two-step melting process: superfluid coherence vanishes first, followed by the loss of crystalline order at higher temperatures. Interestingly, crystalline order temporarily strengthens at intermediate temperatures due to the intricate spin-hole competitions. Our theoretical predictions can be readily tested in the present Rydberg atom array experiments. The investigations of the strongly correlated quantum phases in the bosonic t - J - V model are expected to shed light on the fundamental understanding of doped quantum magnetism [14, 15].

Acknowledgments.— We acknowledge helpful discussion with Yan-Cheng Wang, Dong-Xu Liu, Heng Shen and Xue-Feng Zhang. This work is supported by the Innovation Program for Quantum Science and Technology of China (Grant No. 2024ZD0300100), the National Basic Research Program of China (Grants No. 2021YFA1400900), Shanghai Municipal Science and Technology (Grant No. 25TQ003, 2019SHZDZX01, 24DP2600100). ZY thanks the Scientific Research Project (No. WU2024B027) and the Start-up Funding of Westlake University. The authors also acknowledge the HPC Centre of Westlake University and Beijing PARATERA Tech Co., Ltd. for providing HPC resources.

* zhengyan@westlake.edu.cn

† xiaopeng.li@fudan.edu.cn

- [1] H. Bernien, S. Schwartz, A. Keesling, H. Levine, A. Omran, H. Pichler, S. Choi, A. S. Zibrov, M. Endres, M. Greiner, *et al.*, Probing many-body dynamics on a 51-atom quantum simulator, *Nature* **551**, 579 (2017).
- [2] H. Weimer, M. Müller, I. Lesanovsky, P. Zoller, and H. P. Büchler, A rydberg quantum simulator, *Nature Physics* **6**, 382 (2010).
- [3] G. Semeghini, H. Levine, A. Keesling, S. Ebadi, T.-T. Wang, D. Bluvstein, R. Verresen, H. Pichler, M. Kalinowski, R. Samajdar, *et al.*, Probing topological spin liquids on a programmable quantum simulator, *Science* **374**, 1242 (2021).
- [4] S. Ebadi, T. T. Wang, H. Levine, A. Keesling, G. Semeghini, A. Omran, D. Bluvstein, R. Samajdar, H. Pichler, W. W. Ho, S. Choi, S. Sachdev, M. Greiner, V. Vuletić, and M. D. Lukin, Quantum phases of matter on a 256-atom programmable quantum simulator, *Nature* **595**, 227 (2021).
- [5] A. Mazurenko, C. S. Chiu, G. H. Ji, M. F. Parsons, M. Kanász-Nagy, R. Schmidt, F. Grusdt, E. Demler, D. Greif, and M. Greiner, A cold-atom fermi-hubbard antiferromagnet, *Nature* **545**, 462 (2017).
- [6] L.-M. Duan, E. Demler, and M. D. Lukin, Controlling spin exchange interactions of ultracold atoms in optical lattices, *Phys. Rev. Lett.* **91**, 090402 (2003).
- [7] C. Gross and I. Bloch, Quantum simulations with ultracold atoms in optical lattices, *Science* **357**, 995 (2017).
- [8] Z. Yan, Y.-C. Wang, R. Samajdar, S. Sachdev, and Z. Y. Meng, Emergent glassy behavior in a kagome rydberg atom array, *Phys. Rev. Lett.* **130**, 206501 (2023).
- [9] P. Scholl, M. Schuler, H. J. Williams, A. A. Eberharter, D. Barredo, K.-N. Schymik, V. Lienhard, L.-P. Henry, T. C. Lang, T. Lahaye, A. M. Läuchli, and A. Browaeys, Quantum simulation of 2d antiferromagnets with hundreds of rydberg atoms, *Nature* **595**, 233 (2021).
- [10] C. Chen, G. Emperauger, G. Bornet, F. Caleca, B. Gély, M. Bintz, S. Chatterjee, V. Liu, D. Barredo, N. Y. Yao, *et al.*, Spectroscopy of elementary excitations from quench dynamics in a dipolar xy rydberg simulator, *arXiv preprint arXiv:2311.11726* (2023).
- [11] D. Bluvstein, A. Omran, H. Levine, A. Keesling, G. Semeghini, S. Ebadi, T. T. Wang, A. A. Michailidis, N. Maskara, W. W. Ho, *et al.*, Controlling quantum many-body dynamics in driven rydberg atom arrays, *Science* **371**, 1355 (2021).
- [12] C. Chen, G. Bornet, M. Bintz, G. Emperauger, L. Leclerc, V. S. Liu, P. Scholl, D. Barredo, J. Hauschild, S. Chatterjee, *et al.*, Continuous symmetry breaking in a two-dimensional rydberg array, *Nature* **616**, 691 (2023).
- [13] J. Zhang, S. H. Cantú, F. Liu, A. Bylinskii, B. Braverman, F. Huber, J. Amato-Grill, A. Lukin, N. Gemelke, A. Keesling, *et al.*, Probing quantum floating phases in rydberg atom arrays, *Nature Communications* **16**, 712 (2025).
- [14] A. Bohrdt, L. Homeier, C. Reinmoser, E. Demler, and F. Grusdt, Exploration of doped quantum magnets with ultracold atoms, *Annals of Physics* **435**, 168651 (2021).
- [15] L. Homeier, T. J. Harris, T. Blatz, S. Geier, S. Hollerith, U. Schollwöck, F. Grusdt, and A. Bohrdt, Antiferromagnetic bosonic t - j models and their quantum simulation in tweezer arrays, *Phys. Rev. Lett.* **132**, 230401 (2024).
- [16] X. Lu, F. Chen, W. Zhu, D. N. Sheng, and S.-S. Gong, Emergent superconductivity and competing charge orders in hole-doped square-lattice t - j model, *Phys. Rev. Lett.* **132**, 066002 (2024).
- [17] H.-C. Jiang and T. P. Devereaux, Superconductivity in the doped hubbard model and its interplay with next-nearest hopping t' , *Science* **365**, 1424 (2019).
- [18] A. Auerbach, *Interacting electrons and quantum magnetism* (Springer Science & Business Media, 2012).
- [19] H.-C. Jiang and S. A. Kivelson, High temperature superconductivity in a lightly doped quantum spin liquid, *Phys. Rev. Lett.* **127**, 097002 (2021).
- [20] M. Qiao, G. Emperauger, C. Chen, L. Homeier, S. Hollerith, G. Bornet, R. Martin, B. Gély, L. Klein, D. Barredo, *et al.*, Realization of a doped quantum antiferromagnet with dipolar tunnelings in a rydberg tweezer array, *arXiv preprint arXiv:2501.08233* (2025).
- [21] P. A. Lee, N. Nagaosa, and X.-G. Wen, Doping a mott insulator: Physics of high-temperature superconductivity, *Rev. Mod. Phys.* **78**, 17 (2006).
- [22] J. Koepsell, J. Vijayan, P. Sompet, F. Grusdt, T. A. Hilker, E. Demler, G. Salomon, I. Bloch, and C. Gross, Imaging mag-

- netic polarons in the doped fermi–hubbard model, *Nature* **572**, 358 (2019).
- [23] P. T. Brown, D. Mitra, E. Guardado-Sanchez, R. Nourafkan, A. Reymbaut, C.-D. Hébert, S. Bergeron, A.-M. S. Tremblay, J. Kokalj, D. A. Huse, P. Schauß, and W. S. Bakr, Bad metallic transport in a cold atom fermi-hubbard system, *Science* **363**, 379 (2019).
- [24] J. Koepsell, D. Bourgund, P. Sompet, S. Hirthe, A. Bohrdt, Y. Wang, F. Grusdt, E. Demler, G. Salomon, C. Gross, *et al.*, Microscopic evolution of doped mott insulators from polaronic metal to fermi liquid, *Science* **374**, 82 (2021).
- [25] A. Bohrdt, L. Homeier, I. Bloch, E. Demler, and F. Grusdt, Strong pairing in mixed-dimensional bilayer antiferromagnetic mott insulators, *Nature Physics* **18**, 651 (2022).
- [26] M. Xu, L. H. Kendrick, A. Kale, Y. Gang, G. Ji, R. T. Scalettar, M. Lebrat, and M. Greiner, Frustration-and doping-induced magnetism in a fermi–hubbard simulator, *Nature* **620**, 971 (2023).
- [27] M. Lebrat, M. Xu, L. H. Kendrick, A. Kale, Y. Gang, P. Seetharaman, I. Morera, E. Khatami, E. Demler, and M. Greiner, Observation of nagaoka polarons in a fermi–hubbard quantum simulator, *Nature* **629**, 317 (2024).
- [28] M. Xu, L. H. Kendrick, A. Kale, Y. Gang, C. Feng, S. Zhang, A. W. Young, M. Lebrat, and M. Greiner, A neutral-atom Hubbard quantum simulator in the cryogenic regime, *Nature* [10.1038/s41586-025-09112-w](https://doi.org/10.1038/s41586-025-09112-w) (2025).
- [29] A. W. Sandvik, Stochastic series expansion method for quantum ising models with arbitrary interactions, *Phys. Rev. E* **68**, 056701 (2003).
- [30] O. F. Syljuåsen, Directed loop updates for quantum lattice models, *Phys. Rev. E* **67**, 046701 (2003).
- [31] E. Merali, I. J. S. De Vlugt, and R. G. Melko, Stochastic series expansion quantum monte carlo for rydberg arrays, *SciPost Physics Core* **7**, 016 (2024).
- [32] I. S. Aranson, N. B. Kopnin, and V. M. Vinokur, Dynamics of vortex nucleation by rapid thermal quench, *Phys. Rev. B* **63**, 184501 (2001).
- [33] A. Mitra, Quantum quench dynamics, *Annual Review of Condensed Matter Physics* **9**, 245 (2018).
- [34] Z. Yan, Z. Zhou, Y.-H. Zhou, Y.-C. Wang, X. Qiu, Z. Y. Meng, and X.-F. Zhang, Quantum optimization within lattice gauge theory model on a quantum simulator, *npj Quantum Information* **9**, 89 (2023).
- [35] E. L. Pollock and D. M. Ceperley, Path-integral computation of superfluid densities, *Phys. Rev. B* **36**, 8343 (1987).
- [36] W.-L. You, Y.-W. Li, and S.-J. Gu, Fidelity, dynamic structure factor, and susceptibility in critical phenomena, *Phys. Rev. E* **76**, 022101 (2007).
- [37] D. Schwandt, F. Alet, and S. Capponi, Quantum monte carlo simulations of fidelity at magnetic quantum phase transitions, *Phys. Rev. Lett.* **103**, 170501 (2009).
- [38] A. F. Albuquerque, F. Alet, C. Sire, and S. Capponi, Quantum critical scaling of fidelity susceptibility, *Phys. Rev. B* **81**, 064418 (2010).
- [39] L. Wang, Y.-H. Liu, J. Imriška, P. N. Ma, and M. Troyer, Fidelity susceptibility made simple: A unified quantum monte carlo approach, *Phys. Rev. X* **5**, 031007 (2015).
- [40] A. Andreev and I. Lifshits, Quantum theory of defects in crystals, *Zhur Eksper Teoret Fiziki* **56**, 2057 (1969).
- [41] G. V. Chester, Speculations on bose-einstein condensation and quantum crystals, *Phys. Rev. A* **2**, 256 (1970).
- [42] See supplemental material (2025).
- [43] J. Brooke, D. Bitko, T. F. Rosenbaum, and G. Aeppli, Quantum annealing of a disordered magnet, *Science* **284**, 779 (1999).
- [44] J. Brooke, T. F. Rosenbaum, and G. Aeppli, Tunable quantum tunnelling of magnetic domain walls, *Nature* **413**, 610 (2001).
- [45] C. Chen, G. Bornet, M. Bintz, G. Emperauger, L. Leclerc, V. S. Liu, P. Scholl, D. Barredo, J. Hauschild, S. Chatterjee, M. Schuler, A. M. Läuchli, M. P. Zaletel, T. Lahaye, N. Y. Yao, and A. Browaeys, Continuous symmetry breaking in a two-dimensional rydberg array, *Nature* **616**, 691 (2023).
- [46] A. J. Walker, New fast method for generating discrete random numbers with arbitrary frequency distributions, *Electronics Letters* **10**, 127 (1974).
- [47] A. J. Walker, An efficient method for generating discrete random variables with general distributions, *ACM Trans. Math. Softw.* **3**, 253 (1977).
- [48] M. D. Vose, A linear algorithm for generating random numbers with a given distribution, *IEEE Transactions on Software Engineering* **17**, 972 (1991).
- [49] H. Suwa and S. Todo, Markov chain monte carlo method without detailed balance, *Phys. Rev. Lett.* **105**, 120603 (2010).
- [50] M. E. Fisher, M. N. Barber, and D. Jasnow, Helicity modulus, superfluidity, and scaling in isotropic systems, *Phys. Rev. A* **8**, 1111 (1973).
- [51] B. D. Josephson, Relation between the superfluid density and order parameter for superfluid he near T_c , *Physics Letters* **21**, 608 (1966).
- [52] M. Song, J. Zhao, Y. Qi, J. Rong, and Z. Y. Meng, Quantum criticality and entanglement for the two-dimensional long-range heisenberg bilayer, *Physical Review B* **109**, L081114 (2024).

Supplemental Materials: Double Supersolid Phase in a Bosonic t - J - V Model with Rydberg Atoms

In this Supplemental Material, we describe the SSE-QMC algorithm for the t - J - V model together with the additional results supporting the claim in the main paper.

QUANTUM MONTE CARLO SCHEME

The Hamiltonian of the t - J - V model is

$$\hat{H}_{tJV} = - \sum_{i < j} \sum_{\sigma = \downarrow, \uparrow} \frac{t}{r_{ij}^3} \left(\hat{a}_{i,\sigma}^\dagger \hat{a}_{j,h}^\dagger \hat{a}_{i,h} \hat{a}_{j,\sigma} + \text{h.c.} \right) + \sum_{i < j} \frac{1}{r_{ij}^6} \left[J^z \hat{S}_i^z \hat{S}_j^z + \frac{J^\perp}{2} \left(\hat{S}_i^+ \hat{S}_j^- + \text{h.c.} \right) \right] + \sum_{i < j} \frac{V}{r_{ij}^6} \hat{n}_i^h \hat{n}_j^h. \quad (\text{S1})$$

Here we take $\mu = 0$. We can decompose this Hamiltonian into elementary operators defined on each bond

$$\begin{aligned} \hat{H}_{0,0} &= \mathbb{I}, \\ \hat{H}_{1,b} &= \sum_{\sigma = \downarrow, \uparrow} \frac{t}{r_{ij}^3} \left(\hat{a}_{i,\sigma}^\dagger \hat{a}_{j,h}^\dagger \hat{a}_{i,h} \hat{a}_{j,\sigma} + \text{h.c.} \right), \\ \hat{H}_{2,b} &= - \frac{J^\perp}{2r_{ij}^6} \left(\hat{S}_i^+ \hat{S}_j^- + \text{h.c.} \right), \\ \hat{H}_{3,b} &= - \frac{J^z}{r_{ij}^6} \hat{S}_i^z \hat{S}_j^z - \frac{V}{r_{ij}^6} \hat{n}_i^h \hat{n}_j^h + C_{ij}, \end{aligned} \quad (\text{S2})$$

the r^{-6} terms are truncated at 2 while the r^{-3} terms are truncated at 4 in the unit of lattice spacing. The constant C_{ij} is added to make all matrix elements in $\hat{H}_{3,b}$ non-negative

$$C_{ij} = \begin{cases} \max(|\min(0, -V_{ij}, -|J_{ij}^z|/4)| + \epsilon |\min(0, -V_{ij}, -|J_{ij}^z|/4)|, t_{ij}) & r_{ij} \leq 2 \\ t_{ij} & 2 < r_{ij} \leq 4. \end{cases} \quad (\text{S3})$$

with $V_{ij} = V/r_{ij}^6$, $J_{ij}^z = J^z/r_{ij}^6$ and $t_{ij} = t/r_{ij}^3$, ϵ is a multiplicative constant. Now $\hat{H}_{tJV} = - \sum_{i=1}^3 \sum_b H_{i,b}$ and the partition function $Z = \text{Tr} e^{-\beta H}$ can be expressed as the power series expansion

$$Z = \sum_{\alpha} \sum_{S_M} \frac{\beta^n (M-n)!}{M!} \langle \alpha | \prod_{i=1}^M H_{a_i, p_i} | \alpha \rangle, \quad (\text{S4})$$

with M is the cutoff of the expansion series and S_M represents a particular sequence of n non-identity elementary operators in imaginary time. The matrix elements in S4 are constituted by the single matrix element in the spin σ^z and hole occupation basis

$$\begin{aligned} \langle \uparrow h | \hat{H}_{1,b} | h \uparrow \rangle &= \langle h \uparrow | \hat{H}_{1,b} | \uparrow h \rangle = \langle \downarrow h | \hat{H}_{1,b} | h \downarrow \rangle = \langle h \downarrow | \hat{H}_{1,b} | \downarrow h \rangle = t_{ij}, \\ \langle \uparrow \downarrow | \hat{H}_{2,b} | \downarrow \uparrow \rangle &= \langle \downarrow \uparrow | \hat{H}_{2,b} | \uparrow \downarrow \rangle = -J_{ij}^\perp / 2, \\ W_{ij}^{(1)} &= \langle \uparrow \downarrow | \hat{H}_{3,b} | \uparrow \downarrow \rangle = \langle \downarrow \uparrow | \hat{H}_{3,b} | \downarrow \uparrow \rangle = C_{ij} + J_{ij}^z / 4, \\ W_{ij}^{(2)} &= \langle \uparrow \uparrow | \hat{H}_{3,b} | \uparrow \uparrow \rangle = \langle \downarrow \downarrow | \hat{H}_{3,b} | \downarrow \downarrow \rangle = C_{ij} - J_{ij}^z / 4, \\ W_{ij}^{(3)} &= \langle \uparrow h | \hat{H}_{3,b} | \uparrow h \rangle = \langle h \uparrow | \hat{H}_{3,b} | h \uparrow \rangle = \langle \downarrow h | \hat{H}_{3,b} | \downarrow h \rangle = \langle h \downarrow | \hat{H}_{3,b} | h \downarrow \rangle = C_{ij}, \\ W_{ij}^{(4)} &= \langle hh | \hat{H}_{3,b} | hh \rangle = C_{ij} - V_{ij}, \end{aligned} \quad (\text{S5})$$

where the subscript i, j on matrix elements $W^{(1,2,3,4)}$ contains spatial dependence, which is labeled for further illustration of the updating scheme.

The updating scheme contains two major update: the diagonal update and the directed-loop update, which described as follows:

(1) Diagonal update: The diagonal update follows by visting through through every imaginary time slice $p \in 1, 2, \dots, M$ and either remove or insert a diagonal operator according to the following procedures [31].

(a) For a diagonal operator $\hat{H}_{3,b}$ encountered, remove it ($n \rightarrow n - 1$) with the probability

$$P(n \rightarrow n - 1) = \min\left(\frac{M - n + 1}{\beta\mathcal{N}}, 1\right), \quad (S6)$$

with $\mathcal{N} = \sum_b \max(W_{ij}^{(1)}, W_{ij}^{(2)}, W_{ij}^{(3)}, W_{ij}^{(4)})$ the normalizing factor.

(b) For an identity operator $\hat{H}_{0,0}$ encountered, first decide whether or not to insert ($n \rightarrow n + 1$) the diagonal operator $\hat{H}_{3,b}$ with the probability

$$P(n \rightarrow n + 1) = \min\left(\frac{\beta\mathcal{N}}{M - n}, 1\right). \quad (S7)$$

(c) If the insertion is accepted, then use the Alias method [46–48] to sample from all of the spatial bond according to the distribution $P_b = \max(W_{ij}^{(1)}, W_{ij}^{(2)}, W_{ij}^{(3)}, W_{ij}^{(4)})/\mathcal{N}$.

(d) After select the bond b , read the state at the current imaginary time slice p to evaluate the actual weight of bond $W_{ij}^{\text{actual}} \in [W_{ij}^{(1)}, W_{ij}^{(2)}, W_{ij}^{(3)}, W_{ij}^{(4)}]$. Then insert the operator $\hat{H}_{3,b}$ at bond b with the probability

$$P = \frac{W_{ij}^{\text{actual}}}{\max(W_{ij}^{(1)}, W_{ij}^{(2)}, W_{ij}^{(3)}, W_{ij}^{(4)})} \quad (S8)$$

(e) For an off-diagonal operator $\hat{H}_{1,b}$ or $\hat{H}_{2,b}$ encountered, propagate the state $|\alpha_p\rangle \propto \hat{H}_{1/2,b} |\alpha_{p-1}\rangle$.

(f) Repeat the step (a) at the next imaginary time slice.

(2) Directed-loop update: The directed-loop upate follows by first randomly select one of the vertex legs as an initial entrance leg. Then one need to know the state ($|h\rangle, |\uparrow\rangle, |\downarrow\rangle$) of the entrance leg to proceed.

(a) If the spin state $|\uparrow\rangle$ or $|\downarrow\rangle$ is picked, either flip the spin state or annihilate the spin to create a hole with the probability 1/2 (corresponds to add a ± 1 or ± 2 operator at the entrance leg).

(b) If the hole state $|h\rangle$ is picked, either change the hole to $|\uparrow\rangle$ or to $|\downarrow\rangle$ with the probability 1/2 (corresponds to add a ± 1 operator at the entrance leg).

(c) Choose the exit leg with the probability given by the pre-computed probability. The probability of the exit leg is defined with matrix elements obtained by flipping spins in a vertex and also the insert operator ± 1 or ± 2 . For the detailed construction we refer to [49].

(d) Then the next entrance leg which the exit leg is connected keeps the former step until forming a closed loop.

During our simulations, we found that conventional methods struggled to effectively sample the small- t region. To overcome this challenge, we employed the annealing method [8, 32, 33], where we initialized the system at large- t values and then gradually decreased t through successive simulations. After completing the forward annealing process, we also performed the reverse procedure by gradually increasing t . Interestingly, this approach revealed hysteresis when crossing what appeared to be a first-order phase boundary, as illustrated in Fig. S1.

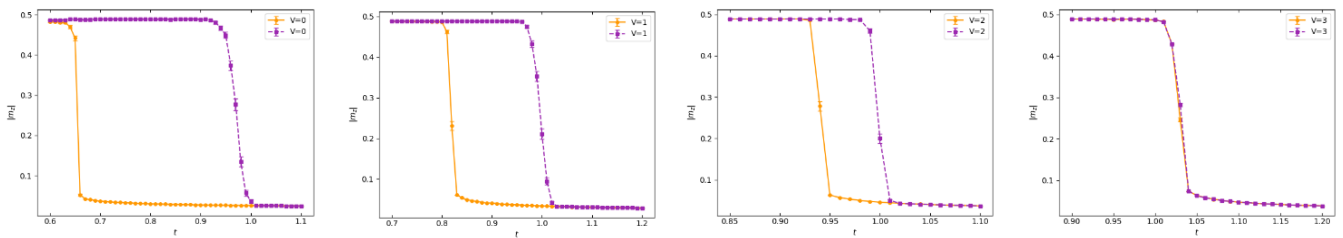


FIG. S1: The hysteresis during the QMC simulations with different V . The yellow solid line is the result from annealing forward and the purple dashed line is result from annealing backward. ($L = \beta = 16$).

As V increases, the hysteresis loop progressively shrinks, indicating that the first-order nature of the phase transition weakens. At $V = 3$, the forward and backward annealing results nearly overlap, suggesting the presence of a tricritical point in this vicinity.

FINITE SIZE SCALING ANALYSIS

We perform finite size scaling analysis of our simulation results. We first investigate the phase transition from the DSS phase to the DSF phase. We consider the Binder cumulant, which is a dimensionless quantity that can be used to locate the quantum critical point

$$U = 1 - \frac{\langle m^4 \rangle}{3\langle m^2 \rangle^2} \quad (\text{S9})$$

with $m = \frac{1}{N} \sum_j e^{-i\mathbf{Q}\cdot\mathbf{r}_j} S_j^z$ and $\mathbf{Q} = (\pi, \pi)$. The results are shown in Fig. S2, as one can see the crossing point locates at $t_c = 1.354(1)$. We further collapse the Néel order parameter $|m_z|$ using the determined t_c according to the finite size scaling relation $|m_z| \cdot L^{\beta/\nu} = f\left[\frac{t-t_c}{t_c} \cdot L^{1/\nu}\right]$ (see Fig. S3). The correlation length critical exponent $\nu = 0.6301$ and the order parameter exponent $\beta = 0.3265$ used to perform data collapse belong to the (2+1) D Ising critical universality, as expected since the van der Waals interaction forming the AFM order is short-ranged.

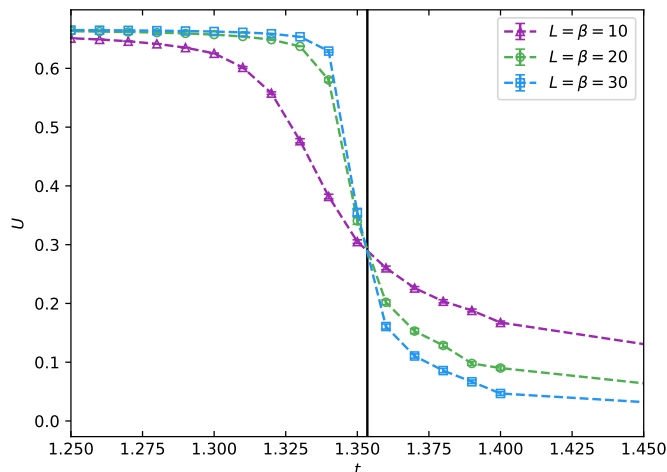


FIG. S2: Binder cumulant as a function of t for different sizes with $V = 8$, the black solid line locates at $t_c = 1.354(1)$.

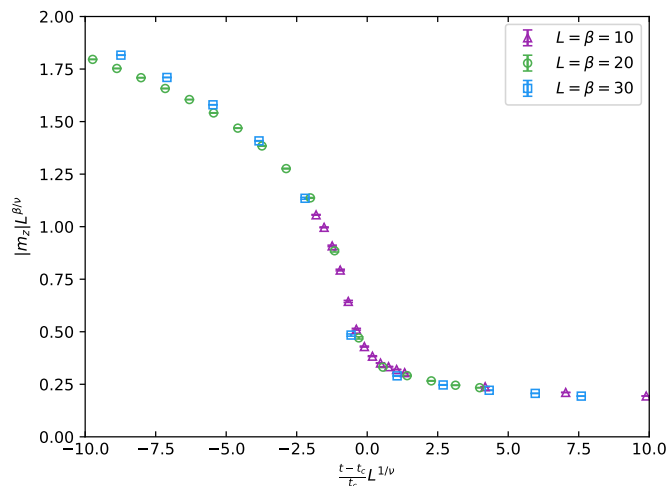


FIG. S3: Data collapse of the Néel order parameter $|m_z|$ near the critical point t_c with critical exponent $\nu = 0.6301$ and $\beta = 0.3265$.

We then consider the phase transition from the AFM phase to the DSS phase, which breaks the $U(1)$ symmetry. The finite

size scaling of the superfluid density [50–52] near the critical point is given by

$$\rho_s L^{d+z-2} = f \left[\frac{t-t_c}{t_c} \cdot L^{1/\nu'} \right], \quad (\text{S10})$$

with $\nu' = \nu \frac{d_{uc}}{d}$, $d = 2$ is the dimension of system and $d_{uc} = \frac{3}{2}(\alpha - d)$ is the upper critical dimension, $z = 1$ is the dynamical critical exponent. The result is shown in Fig. S4, where $L\rho_s$ is size independent at the critical point.

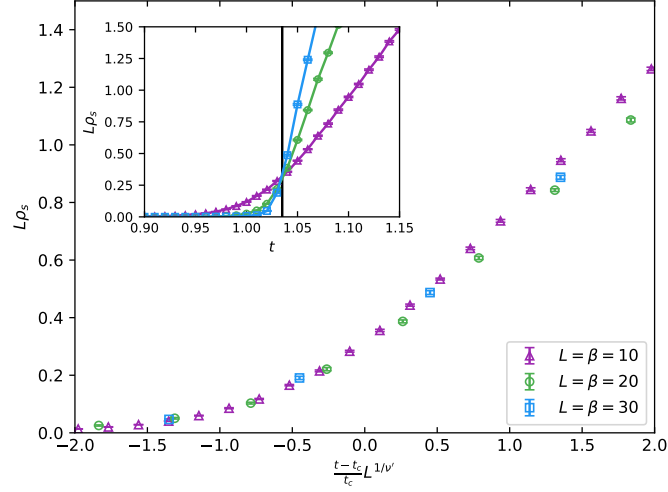


FIG. S4: Data collapse of the superfluid density according to S10 with critical exponent $\nu' = \nu \frac{d_{uc}}{d} = 0.75$. The inset shows the curves for $L\rho_s$ for different system sizes near the critical point t_c , the black solid line locates at $t_c = 1.035(1)$.

However, due to the truncation of long-range interactions and the presence of two $U(1)$ symmetries, the current data do not provide clear evidence that the AFM-to-DSS phase transition is continuous. We leave this question for future investigation.

Finally, we consider the finite temperature transition that melts the AFM phase to the disordered phase in Fig. 5, we plot the scaled reduced structure factor $S(\pi, \pi)L^{2\beta/\nu}/N$ for different system sizes (neglect the $L = 10$ case due to the strong finite size effect) as shown in Fig. S5. The universal crossing point indicate that it is a 2D Ising transition with critical temperature $T_c = 1.131(2)$.

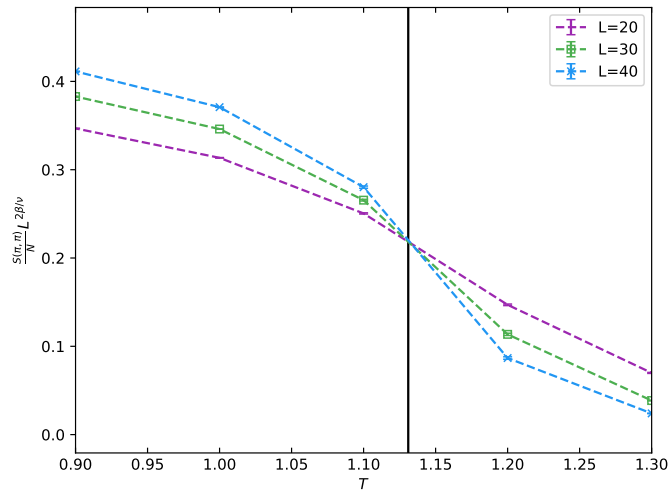


FIG. S5: Finite size scaling of the reduced structure factor $S(\pi, \pi)/N$. Curves for $S(\pi, \pi)L^{2\beta/\nu}/N$ for different system sizes near the critical point T_c with $2\beta/\nu = 0.25$, the black solid line locates at $T_c = 1.131(2)$. $V = 8$ and $t = 1.2$.

SUPERFLUID DENSITY OF SPIN PART

We examine the superfluid density associated with the spin component, following the same definition of the hole part

$$\rho_s^{\uparrow/\downarrow} = \frac{L^{2-d} \langle W_{x,\uparrow/\downarrow}^2 + W_{y,\uparrow/\downarrow}^2 \rangle}{2d\beta t}, \quad (\text{S11})$$

where $W_{x,\uparrow/\downarrow}$ and $W_{y,\uparrow/\downarrow}$ here refer to the winding numbers of the spin up/down in the x - and y -directions. For the AFM-to-DSS transition the result is shown in Fig S6.

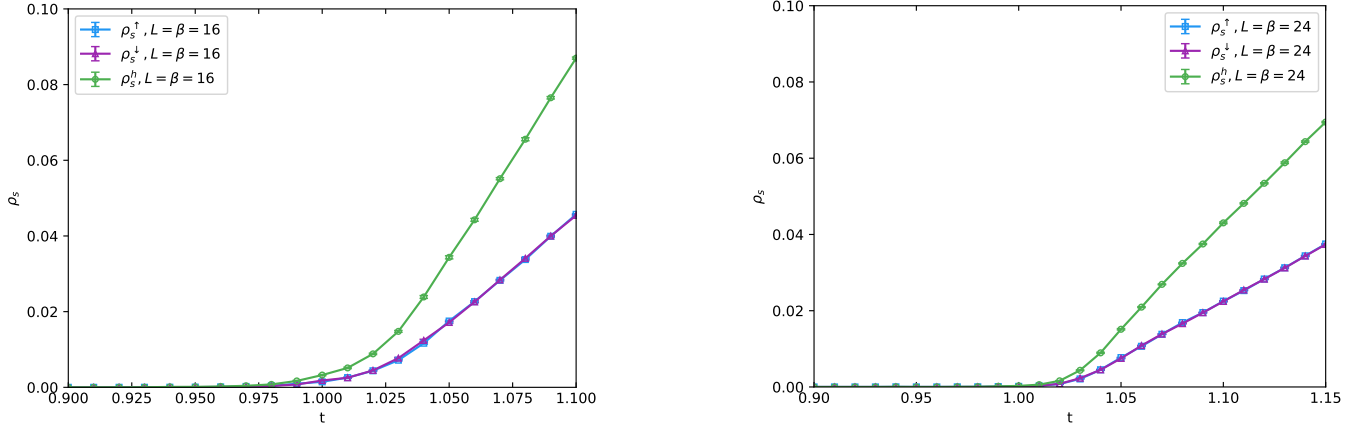


FIG. S6: Superfluid density as functions for different t associated with spin up, spin down and hole respectively. The left figure is $L = 16$ result and the right figure is $L = 24$ result. $V = 8$.

To confirm that spin superfluidity also vanishes during the thermal phase transition, we present measurements in Fig. S7, which demonstrate that both spin-up and spin-down superfluid densities follow behavior similar to the hole superfluid density, consistently diminishing around the same transition temperature.

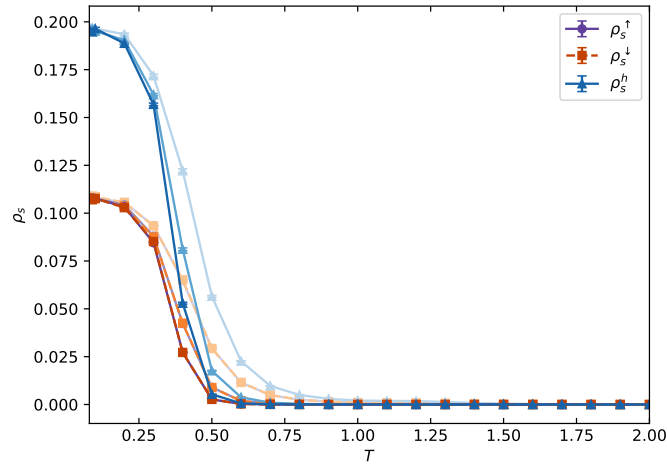


FIG. S7: Superfluid density as a function of temperature T for spin-up, spin-down, and hole components. The color gradient from light to dark indicates increasing system sizes ($L = 20, 30, 40$). Here, $t = 1.2$ and $V = 8$.

BOSONIC HOLES DENSITY

In Fig. S8, we plot the hole density $\rho = \frac{1}{N} \langle \sum_j \hat{n}_j^h \rangle$ for the same parameters in Fig. 3. The hole density ρ vanishes deep inside the small t region, which leads to the effective pure spin-1/2 model with $\hat{H}_J = \sum_{i<j} \frac{1}{r_{ij}^\beta} \left[J^z \hat{S}_i^z \hat{S}_j^z + \frac{J^\perp}{2} (\hat{S}_i^+ \hat{S}_j^- + \text{h.c.}) \right]$.

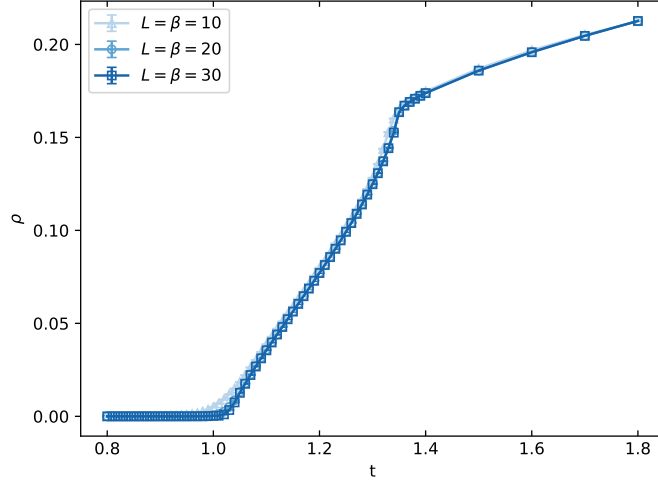


FIG. S8: The hole density ρ as a function of the tunneling strength t for various system sizes. $V = 8$.

In Fig. S9, we plot the density-density correlations of bosonic holes:

$$C^b(\mathbf{r}) = \frac{1}{N} \sum_i [\langle n_i^h n_{i+\mathbf{r}}^h \rangle - \langle n_i^h \rangle \langle n_{i+\mathbf{r}}^h \rangle]. \quad (\text{S12})$$

along the x direction in the DSS and DSF regions. Apart from the nearest-neighbor point—where a pronounced blockade effect dominates— $C^b(\mathbf{r})$ decays rapidly to zero, consistent with a uniform density profile.

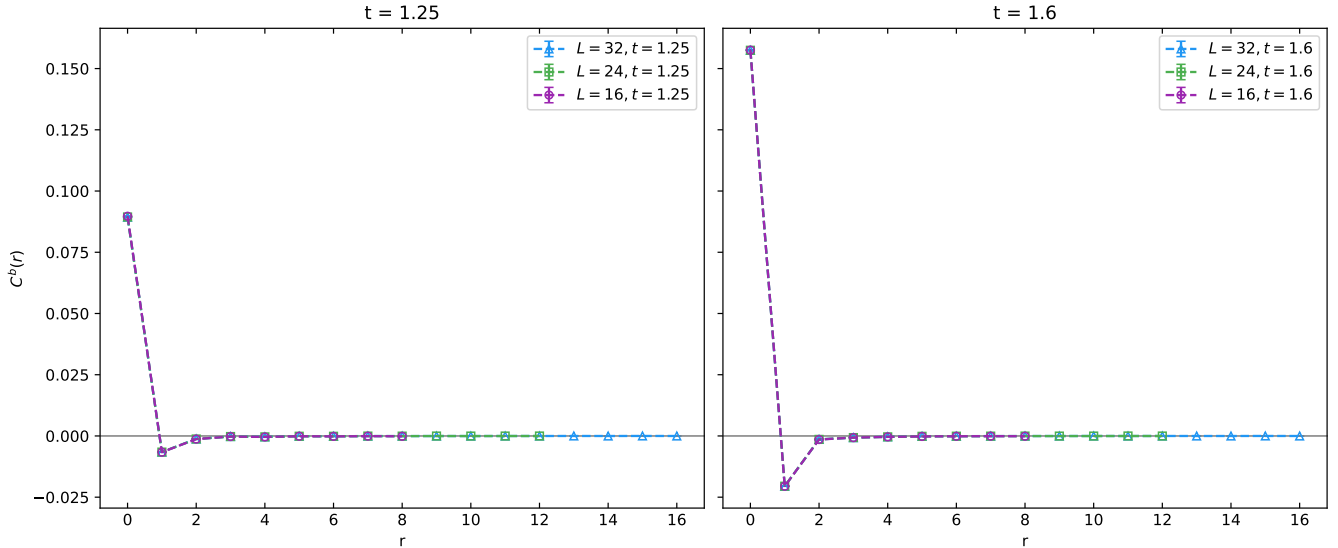


FIG. S9: The hole density-density correlations $C^b(\mathbf{r})$ along the x -direction, $\mathbf{r} = (r, 0)$, are shown in the DSS region (left panel, $t = 1.25$) and in the DSF region (right panel, $t = 1.6$). The hole-hole repulsion strength is set to $V = 8$.